APPLIED SCIENCES AND ENGINEERING

Multiangle, self-powered sensor array for monitoring head impacts

Lulu Zu[1,2]†, Jing Wen[1,2]†, Shengbo Wang[1,2], Ming Zhang[3], Wuliang Sun[1], Baodong Chen[1,2]*, Zhong Lin Wang[1,2,4]*

Mild concussions occur frequently and may come with long-term cognitive, affective, and physical sequelae. However, the diagnosis of mild concussions lacks objective assessment and portable monitoring techniques. Here, we propose a multiangle self-powered sensor array for real-time monitoring of head impact to further assist in clinical analysis and prevention of mild concussions. The array uses triboelectric nanogenerator technology, which converts impact force from multiple directions into electrical signals. With an average sensitivity of 0.214 volts per kilopascal, a response time of 30 milliseconds, and a minimum resolution of 1.415 kilopascals, the sensors exhibit excellent sensing capability over a range of 0 to 200 kilopascals. Furthermore, the array enables reconstructed head impact mapping and injury grade assessment via a prewarning system. By gathering standardized data, we expect to build a big data platform that will permit in-depth research of the direct and indirect effects between head impacts and mild concussions in the future.

INTRODUCTION

A mild concussion that can result from impacts or jolts to the head is a critical risk factor for dementia, Alzheimer's disease, and other neurodegenerative diseases (*1*). An estimated 42 million people worldwide suffer from mild concussions each year, particularly in sports represented by skiing, American football, and boxing (*2*, *3*). The patient's self-reported symptoms are the only source of information for the diagnosis of mild concussions. Moreover, traditional imaging techniques such as computerized tomography and magnetic resonance imaging play a little role in the diagnosis, because mild concussion typically does not lead to organic lesions. Clinicians have few objective and trustworthy diagnostic criteria or tools other than their own experience to assess the severity of patients, which makes the diagnosis of mild concussion a key obstacle (*4*, *5*).

With the development of wearable electronics, these devices based on objective data that realize the interaction of sensing and information analysis may become the most efficient and convenient health assessment instruments (*6*). The medical community agrees that energy transfer caused by oblique and vertical impacts to the head is the primary cause of concussion. Many companies have attempted to use acceleration values provided by wearable rigid sensors to determine the onset of mild concussions. However, the human head kinematics relevant to mild concussions are determined by the magnitude, direction, and position of the external force. Moreover, the severity and long-term effects of repetitive concussions in the same position are alarming. Therefore, there is in demand for intensity and position analysis of head impacts rather than simple threshold alerts. Various flexible pressure sensors, such as piezoelectric, piezoresistive, and capacitive sensors, offer a wide detection range but low sensitivity and remain challenged by materials and energy sources (*7*, *8*). Triboelectric nanogenerator (TENG), originating from the coupling of the triboelectrification effect and the electrostatic induction, has attracted much attention for its characteristics of self-powered sensing, high sensitivity, and material diversity (*9*–*15*). TENG, which can convert mechanical energy generated by two different materials into electrical signals with rather high magnitudes, is an ideal candidate for providing active sensing of static and dynamic pressure (*16*–*19*). However, the TENG as an emerging sensor still lacks a standard production process, and the laboratory's handmade products make its large-scale application a major challenge. Advances in three-dimensional (3D) printing technologies have enabled the standardization of sensors produced from various materials, such as conductors (*20*), semiconductors (*21*, *22*), and biomaterials (*23*), and adapted to irregular body structures. Combining the 3D printing technology not only simplifies the processing of TENGs and reduces costs but also allows for one-piece integration into a variety of application scenarios (*24*–*26*). 3D printing suggests a feasible route for commercialization of TENG and demonstrates excellent promise in the personalized medicine (*27*, *28*), smart sports (*29*), and aerospace.

Here, we propose a strategy to achieve effective monitoring of head impacts by a softly curved sensing array consisting of fully 3D printed multiangle TENGs (MA-TENGs). Inspired by metamaterial structure, MA-TENG allows converting forces from multiple directions such as compression, rotation, and shearing into electrical signals during impact without a power supply. In addition, our design incorporates 3D scanning to create an array of curved surfaces that better fit the natural shape of the human head. On this basis, we integrated a head impact remote sensing (HIRS) system that encodes the pulse signal into a color mapping to report the impact pressure and position to the terminal. Assisted by machine learning algorithms, it also demonstrated the assessment of injury grades (accuracy of 98%). Moreover, the soft topology can reduce the impact energy transfer to the brain within a certain range, which plays a positive protective role against mild

[1]Beijing Institute of Nanoenergy and Nanosystems, Chinese Academy of Sciences, Beijing 101400, P. R. China. [2]School of Nanoscience and Technology, University of Chinese Academy of Sciences, Beijing 100049, P. R. China. [3]Senior Department of Cardiology, The First Medical Center of PLA General Hospital, Beijing 100853, P. R. China. [4]Georgia Institute of Technology, Atlanta, GA 30332-0245, USA.
*Corresponding author. Email: chenbaodong@binn.cas.cn (B.C.); zhong.wang@mse.gatech.edu (Z.L.W.)
†These authors contributed equally to this work.

concussions. Briefly, this work measures and visualizes head impact, offering a trustworthy method for more in-depth analysis and prevention of mild concussions.

RESULTS

Principle and properties of MA-TENG

Energy transfer from different types of impacts to the head can cause shearing, compression, rotation, and tearing of the brain within the skull, resulting in mild concussions (Fig. 1A). A wearable sensing array is designed to enable wireless location tracking and grade assessment of head impacts (Fig. 1B). The array consists of 32 MA-TENG units (30 mm by 30 mm by 9 mm) in a configuration that comprises an elastic hemisphere made of treated thermoplastic polyurethane (T-TPU material), a multiangle spring made of 3D printed TPU (P-TPU material), a flexible electrode made of conductive TPU (C-TPU material), and two hexagonal substrates made of P-TPU on the top and bottom (Fig. 1C). Compared to other bulky and intricately wired solutions, the device is lighter, more flexible, and portable. The initial deformation can be triggered by tiny forces due to the low Young's modulus of the 3D printed material (Fig. 1D). A scanning electron microscope (SEM) photograph of the connection between the C-TPU and P-TPU materials is shown in Fig. 1E. The two materials have a great articulation, which allows us to print different materials at once to create more intricate structures. The change in simulated strain (Fig. 1F) is plotted as MA-TENG is stressed at different angles (movie S1).

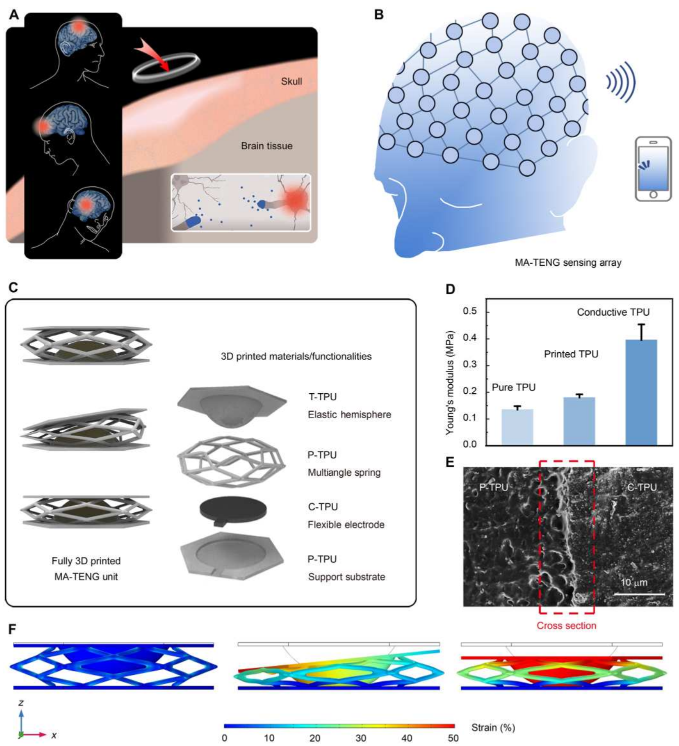

Fig. 1. Concepts, structure, and properties of MA-TENG. (**A**) Basic concepts interpretation of mild concussions caused by different types of head impacts. (**B**) Schematic of a wearable "MA-TENG sensing array" which provides real-time monitoring of head impact by wireless position tracking and grade assessment. (**C**) Exploded view of the fully 3D printed MA-TENG, which can be compressed, sheared, and rotated. (**D**) Young's modulus of MA-TENG's 3D printing material. (**E**) SEM image of the P-TPU and T-TPU materials. (**F**) Strain simulation of MA-TENG under different angular stresses.

On the basis of the structural design of multiangle transformation, TENG with different working modes can be manufactured. The MA-TENG will operate in single-electrode mode to meet the practical needs of head-mounted. Single-electrode mode means that another contact surface is allowed to move at multiple angles without the constraints of the wire (fig. S1), and the C-TPU part will perform as an electrode connected to the external load via a wire. The working principle of MA-TENG in single-electrode mode is shown in Fig. 2A. After the electrode contacts the elastic hemisphere, it acquires a negative triboelectric charge because T-TPU has a stronger capacity to capture negative charges, while the C-TPU leaves a positive charge (I). Once the elastic hemisphere begins to separate from the electrode, the potential difference between the two surfaces will gradually increase, causing a directed flow of electrons in the external circuit from the ground to the C-TPU electrode (II). Up until the elastic hemisphere and electrode are completely separated, this transient current persists (III). As the elastic hemisphere approaches the electrode once more, electrons will be repelled from the electrode by external loads back to the ground (IV). The MA-TENG will be able to constantly transform mechanical energy into alternating current electrical signals through repeated contact-separation motions between the two interfaces. The potential distribution of electrode surface was analyzed using a potential scanner (Fig. 2B) and compared for different shapes of electrodes (fig. S2). As can be seen, electrode has the largest contact area and most potential when it is a plane. The stress distribution of the section is depicted in Fig. 2C using the finite element simulation (COMSOL). The MA-TENG transitioned from point contact (state I) to surface contact (state II) as the pressure increased, and its contact area gradually increases (Fig. 2D). In particular, two distinct linear zones were visible around 50 kPa, which coincided with the data obtained during experiment. The common sensitivity partitioning phenomena in TENG sensors is thought to be caused by the differing ratios of contact area expansion in low-pressure and high-voltage regions. In the low-pressure region, a small contact area can cause a notable change in the separation distance; in the high-pressure region, the contact surface is flattened, and the change in the separation distance decreases. The separation distance determines the voltage value (*30*), and different voltage increases bring different sensitivities. Theoretically, the voltage of MA-TENG can be approximately expressed as follows (see text S1 for details)

$$V_{\mathrm{oc}} = \frac{\sigma_{\mathrm{u}}}{\pi\varepsilon_0}\int_{Z_2-Z_1}^{0} f(z')dz' - \frac{\sigma_{\mathrm{u}}}{\pi\varepsilon_0}\int_{0}^{Z_1-Z_2} f(z')dz' + \frac{\sigma_{\mathrm{t}}}{\pi\varepsilon_0}\int_{0}^{Z_2-Z_3} f(z')dz' - \frac{\sigma_{\mathrm{t}}}{\pi\varepsilon_0}\int_{Z_1-Z_2}^{Z_1-Z_3} f(z')dz' \quad (1)$$

where σ_{u} represents the induced charge density, σ_{t} represents the triboelectric charge density, ε_0 represents the dielectric constant, and z represents the separation distance.

Appropriate structure not only helps our sensors to exhibit the best performance but also gives the MA-TENG the ability to convert to multiple forms. The MA-TENG can harvest forces from different directions and identify shear, rotational, and compressive forces (fig. S3) by amplitude and waveform under the

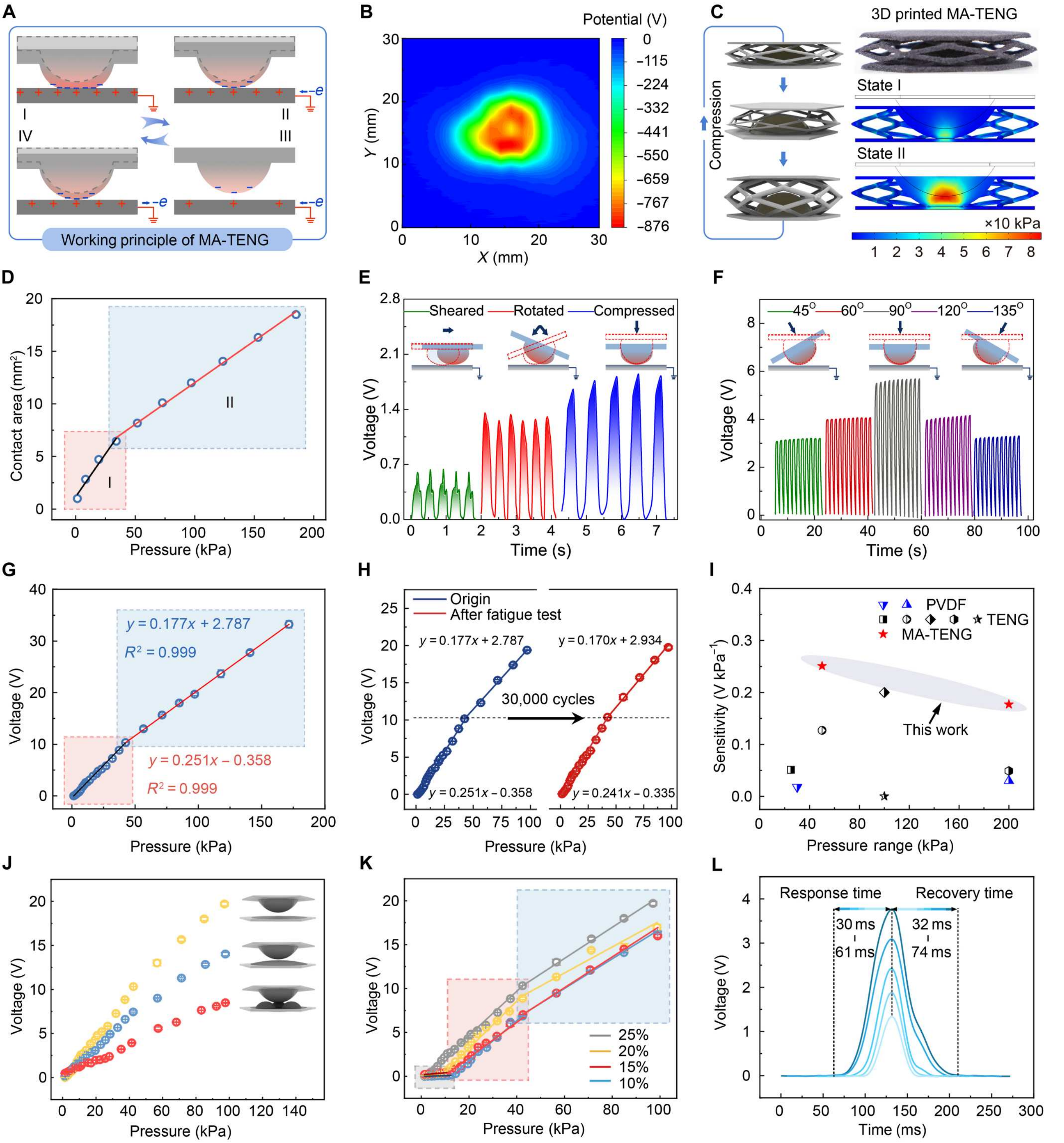

Fig. 2. Principle and properties of MA-TENG. (**A**) Working principle of MA-TENG under one working cycle. (**B**) Potential distribution of the electrode surface after the cycles of 10 contact-separation motions. (**C**) Stress distribution of MA-TENG's hemispherical sections in different states by finite-element simulation. (**D**) Relationship of the contact area and pressure on the elastic hemisphere by finite-element simulation. (**E**) MA-TENG can identify shear, rotational, and compressive forces by the amplitude and waveform of the signal. (**F**) Signals of MA-TENG for different angular stresses at the same force. (**G**) Relationship between the output voltage of MA-TENG and pressure, as well as its linear fitting results. Error bars indicate SDs for three sets of data points. (**H**) Stability test: the effect on sensitivity with 30,000 cycles. (**I**) Comparison of the sensitivity with other pressure sensors. (**J**) Effect of the electrode shape on the output voltage. (**K**) Effect of 3D printed density on the output voltage. (**L**) Response time and recovery time of the sensing signals.

same conditions (Fig. 2E). In particular, when the MA-TENG was fixed at different rotation angles, its voltage signal of angular stress showed notable differences (Fig. 2F). To standardize the output performance of MA-TENG, we used a linear motor to simulate the applied pressure. At the motor's moving end, a dynamometer is permanently mounted. During the process of detecting the pressure and electrical output signals, the dynamometer's probe makes contact with the MA-TENG. The linear fitting curve of voltage value with pressure variation is shown in Fig. 2G. The sensitivity of the sensor is 0.251 V kPa^{-1} (linearity R^2 = 0.999) in the middle and low-voltage section (red area) and 0.177 V kPa^{-1} (linearity R^2 = 0.999) in the high-voltage section (blue region). The results of the fitting demonstrate that the electrical output and pressure of MA-TENGs have an excellent linear relationship. The overall sensitivity declined by just 4% after 30,000 working cycles, as shown in Fig. 2H, demonstrating the superior stability of MA-TENG. In addition, our sensor exhibits ultrahigh sensitivity and ultrawide pressure bandwidth, outperforming other triboelectric and piezoelectric pressure sensors that have been reported in the literature (Fig. 2I) (*31–37*).

The optimization process of the parameters is as follows: We created electrodes with various numbers of contacts to explore the impact of electrode shape on output signal. The flattest electrode form results in the highest sensitivity and maximum output voltage (Fig. 2J; detailed data are available at figs. S4 and S5). In addition, we investigated how printing density affected sensitivity (Fig. 2K). The higher the density, the harder the material, the faster the rebound, the lower the hysteresis. Consequently, we avoided selecting forms with too little density. The effect of different hemisphere heights on response time is shown in Fig. 2L. In terms of reliability, we also compared the signals under single shock and repeated vibrations (fig. S6), which showed consistency. Next, we measured the voltage output of the MA-TENG at various ambient temperatures (fig. S7) and humidity (fig. S8). Although the voltage value decreases with the increase in temperature and humidity, as a sensor, the characteristic trend of MA-TENG is still consistent within a certain range. This is demonstrated by the fact that it remains the same sensitivity and accuracy for pressure recognition over 3 months (fig. S9). In conclusion, the six sensing factors (stability, homogeneity, linearity, repeatability, sensitivity, and hysteresis) were used to evaluate the sensor's overall performance, and the excellent sensing properties of MA-TENG matched the application requirements.

Sensing array color mapping

The photo of fabricated 16-units soft, planar MA-TENG sensing array is shown in Fig. 3A, which the manufacturing method, size, and spacing are all the same for every unit. Note that the accuracy of the sensors array will be affected by the frequent issue of cross-talk between many sensor units and electrode lines. Therefore, we make the electrode wires into a flexible print circuit board (flex-PCB) and set up the upper and lower copper shields to reduce or minimize the effects of cross-talk (all data acquisition below is based on this design). All pixels are connected to the multichannel measurement system and are coded from "A1" to "D4" for electrical response measurement. The apex of each channel's electrical response curve will line up with the coordinate's local pressure response. The applied pressure is controlled by the stepping motor program, and the target contact points are pre-set at different coordinate positions. After applying pressure, the array of preloaded contact points can be imaged as letters "L," "X," and "N" by the rainbow color maps (Fig. 3B). Previous experimental results have shown that the signal amplitude of MA-TENG is affected as the relative humidity (RH) increases. To correct this bias, we measured the sensitivity of the MA-TENG at different RH values. The sensor's sensitivity remains stable over a range with a variable rate of 2.4% (fig. S10A). On the basis of this result, we can further calibrate the readings of the sensor array. Each unit in the array is numbered, and their voltage values are measured at the same pressure (fig. S10B). With RH compensation, the MA-TENG array allows for consistent L load mapping to be reproduced at different RH values (fig. S10C). This ensures that the array has a more accurate determination of the pressure distribution. One step closer to achieve the objective of curved surface sensing has been made with the successful demonstration of planar array pressure distribution. There are few reports on creating pressure sensors on curved surface, and the complex curvature of the head determines that the sensing device must have accurate surface geometry and stability. Therefore, we adopt reverse engineering procedures. First, 3D scanning is used to create the head point cloud. The point cloud is merged with MA-TENG using 3D modeling software and then 3D printed a soft array that approximates the contours of the human head and is ergonomic (Fig. 3C). When the curved sensing array is affected, a series of voltage signals are generated (Fig. 3D). Since these voltage signals correspond to 3D spherical coordinates, the distribution of forces on the curved surface can be seen more intuitively by color mapping (Fig. 3E).

To simulate the actual impact, we built a test platform. The sensing array must acquire a beginning velocity and fall along the track, and its final falling velocity (i.e., the initial velocity upon impact) can be controlled by adjusting the falling height. Regarding the tolerance limits of the head, researchers presented a Wayne State Tolerance Curve (WSTC) in 1963. The results of this study indicated that the peak impact acceleration of the head after wearing the helmet exceeds 100 g and lasts for more than 5 ms, causing fracture of the skull and concussion (fig. S11). On the other hand, a mild concussion could happen at 60 g (*38*). Compared with accelerometers placed in the head model, the peak values of the two parameters were 4.4 and 4.9 ms, respectively (Fig. 3F). MA-TENG absorbs a portion of energy during impact because of the flexibility of the material, resulting in response delay. The recorded pressure readings can be translated to acceleration at various collision speeds using Newton's second law. Figure 3G depicts the fitted linear curve after comparing the translated acceleration with the *g* value simultaneously measured by the accelerometer. The linear equations for the two approaches are $y = 11.581x + 27.723$ (accelerometer) and $y = 10.734x - 26.744$ (MA-TENG), respectively. Similarly, the absorption of energy by MA-TENG causes the difference in intercept between the two equations. Energy absorption has a positive preventive effect on mild concussion, which can reduce energy transfer to the brain under low-, medium-, and high-speed impact. To reduce the deviation, we recalibrate the acceleration of the whole system by complementing the intercept. The impact is regarded as having a risk of mild concussion when the MA-TENG exceeds 7 g (i.e., the accelerometer is 63.9 g). Figure 3H shows the maximum pressure corresponding to each acceleration. In the following sections, we will continue to use these pressure values to assess the injury grade.

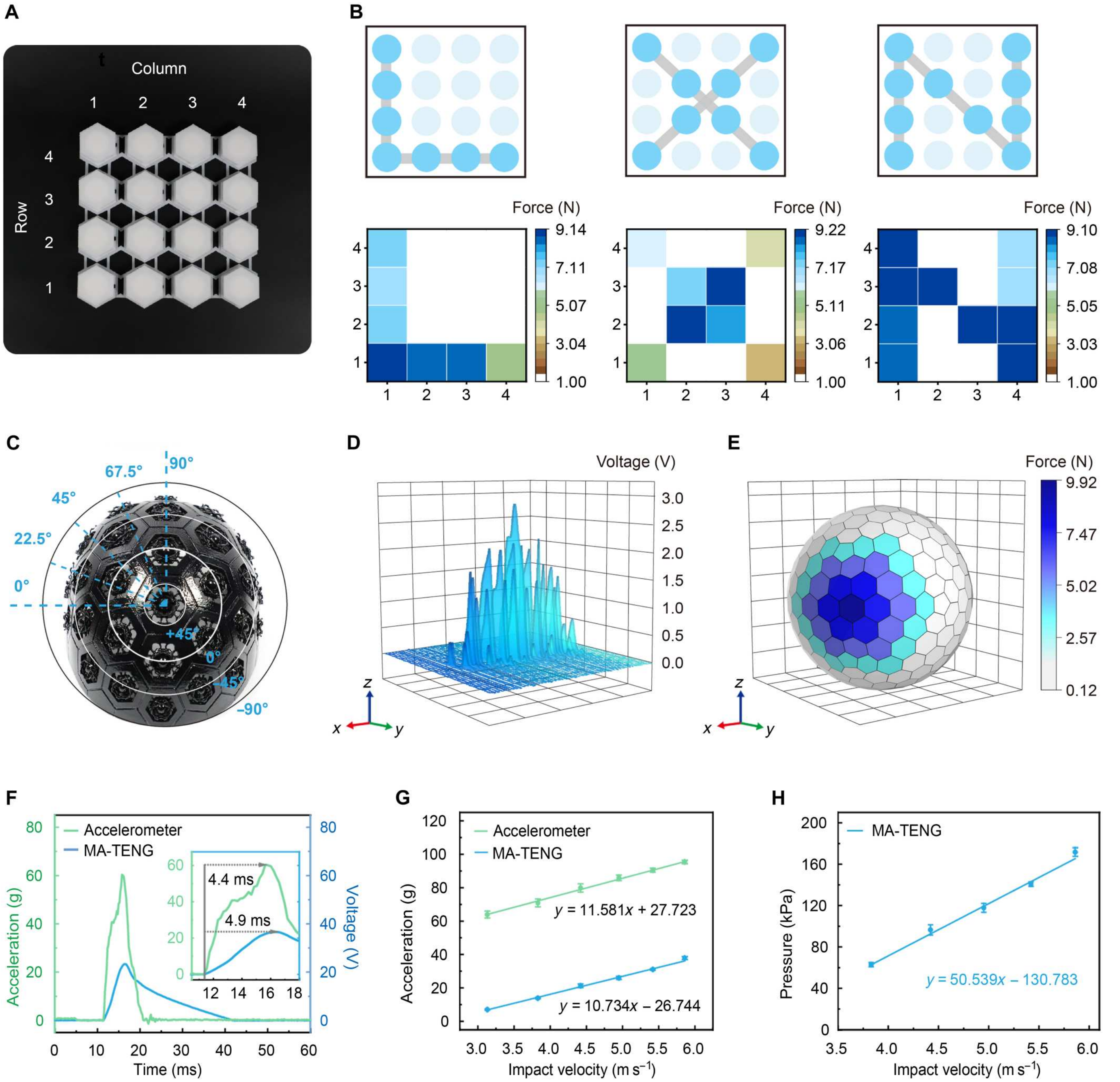

Fig. 3. Sensing array performances and color mapping. (**A**) Photograph of 4 pixel–by–4 pixel planar MA-TENG array. (**B**) Top: The path of the applied impact force, shown as the letters L, X, and N. Bottom: Rainbow color mapping of the impact force corresponding to the voltage output. (**C**) Top view of curved surface MA-TENG array, which the coordinates of each unit positioned by latitude and longitude angles. (**D**) Open-circuit voltage of curved surface MA-TENG array when 37 points are under impact force. (**E**) The voltage values (D) correspond to the color mapping of 3D sphere. (**F**) The pulse signals from the accelerometer (green) and the MA-TENG (blue) at the same impact condition, and the inset shows the amplification of the signals. (**G**) Acceleration values from the accelerometer (green) and the MA-TENG (blue) at different impact conditions and linear fitting results. (**H**) Linear relationship of impact velocity and impact force.

Grading assessment of head impact

For precise assessment of head impact, we analyze and identify multidimensional and vast data by using Deep Convolutional Neural Network (DCNN) (Fig. 4A). The fully connected multilayer perceptron that the DCNN implement can predict one or more response variables and has achieved remarkable success in model prediction. The data generated by the MA-TENG sensing array during the impact process is aggregated by an integrated PCB (Fig. 4B). We divided the interval where mild concussion occurred (60 to 100 g) into grade = 0 to 5 (G0 to G5) according to WSTC criteria. Before modeling operations, we need to clean and extract features from the massive amount of data. We analyzed the correlation

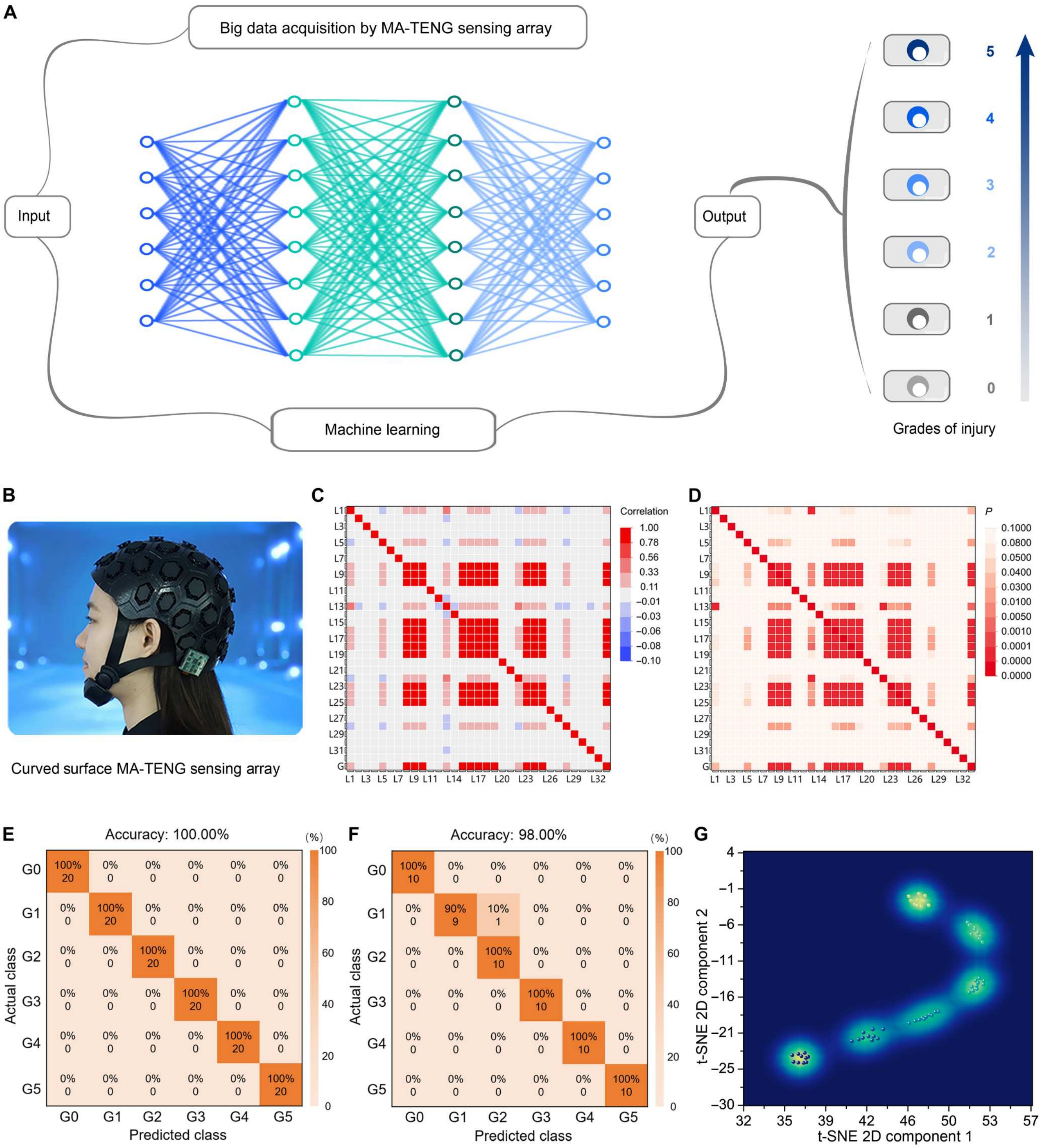

Fig. 4. Grading assessment of head impact based on DCNN algorithm. (**A**) Conceptual diagram of DCNN for injury grade classification. (**B**) Photo of curved surface MA-TENG sensing array. (**C**) Correlation heat map of the data. (**D**) Significant level heat map of the data. (**E**) Confusion matrix of the training set (accuracy of 100%). (**F**) Confusion matrix of the prediction set (accuracy of 98%). (**G**) t-SNE analysis of the prediction set and training set.

(Fig. 4C) between the change value of each channel (L1 to L32) and the injury grades (G0 to G5). This matrix summarizes the strength of the linear relationship between the two sets of response indicator variables. We found that only 16 channels were correlated with injury grade and had a synergistic contribution to grades. The results show that most of the channels are positively correlated with each other (red area), and only a few are negatively correlated (blue area). To verify its accuracy, we again assumed that there is no linear relationship between the two response variables (i.e., P values) and that the true correlation between each P value and the variable is 0. The significant level results (Fig. 4D) showed that there was no negative correlation between the channels ($P > 0.05$) and that the 16 channels remained significantly positively correlated with the injury grade ($P < 0.05$), which is consistent with our previous analysis. We also provide the raw data tables corresponding to the two matrix heat maps (tables S1 and S2) to view the data in more detail. Last, we analyzed the main effects for each channel (text S2), eliminating data that did not have a significant effect on the prediction and obtaining the order of the degree of effect. The model was successfully constructed and correctly classified following training (table S3). The sixfold cross-validated confusion matrix following training (Fig. 4E) and the projected (Fig. 4F) outcome confusion matrix showed great predictive ability. As can be observed, the trained model has a 100% classification accuracy for the injury grade and a 98% prediction accuracy for the prediction set. The specific calculation of the two-layer array is shown in eq. S1. To better visualize the relationship between the predicted data and the training set samples, the data were dimensioned using the t-distributed Stochastic Neighbor Embedding (t-SNE) algorithm. The distribution of the data after dimensionality reduction is shown in Fig. 4G. The shaded part is the distribution area of the training set, and the scattered points are the distribution of the predicted data. The data in the training set become obviously scattered in six categories, while the predicted data are more concentrated and distributed in each shaded part. As a result, the analysis of t-SNE intuitively shows the excellent classification performance of the model and proves the effectiveness of the model prediction.

HIRS system

With objective and reliable assessment criteria, the MA-TENG sensing array and matching DCNN algorithm enable real-time wireless visual monitoring of head impacts in sports such as skating, skiing, boxing, baseball, and motorcycling (Fig. 5A). An HIRS system was proposed with the mobility needs of portable devices in mind. The HIRS system consists of MA-TENG sensing array, data processing module, and mobile terminal. In addition, a supporting structure that has been topologically optimized is added to work with the MA-TENG sensing array to create a smart helmet (Fig. 5B) that is better suited to reducing the effects of mild concussion. The data processing module is a PCB circuit with an integrated signal microcontroller and Bluetooth chip in a low-power design. The PCB is approximately the size of a coin at 28 mm by 30 mm and is powered by a coin cell. The cross-talk–reducing design of flexible PCB serves as a wire to connect the MA-TENG sensing array to the data processing module. The scheme diagram of the HIRS system is shown in Fig. 5C. The signal produced by the MA-TENG sensing array goes to the charge amplifier when the user's head is affected. The semiconductor analog switch transforms the electrical signal into a digital signal that is embedded in the microcontroller in channel order as the analog signal passes through it. The Bluetooth module transmits the converted digital signal to the smartphone in less than 1 s (detailed workflow in fig. S12). Last, the phone can reconstruct the pressure distribution and color grade map during head impact in the application software interface. During this period, the operating voltage of 1.8 V generates an average current consumption of 240 μA and a power consumption of 0.43 mW. Figure 5 (D to F) shows application scenarios and software screenshots for assessing injury risk under different states using the HIRS system. Under mild impact, a total of two points reached the injury grade of G2 with point pressures of 59 and 57 kPa and mainly involved the parietal and frontal bone regions (movie S2). Under severe impact, one point reached the injury grade of G5 with a point pressure of 166 kPa and mainly involved the frontal bone, parietal bone, and occipital bone regions (movie S3). Figure 5 (G and H) shows the 2D rainbow color maps of head impact with representing of injured grades and locations. The results demonstrated that the HIRS system can quickly pinpoint the area of injury before clinical diagnosis of a mild concussion and offer precise and intuitive advice. The advantage lies in the potential reduction of incidents that delay diagnosis and treatment.

DISCUSSION

In this work, we demonstrated a triboelectric sensing method for high-efficiency monitoring and grading assessment of head impact via a fully 3D printed self-powered sensing array. MA-TENG can capture vector information of impact force from multiple directions with high sensitivity and wide detection range. Benefited from the metamaterial structural design and optimized 3D printed materials, the flexibility, stability, and sensitivity of MA-TENG are improved. With an average sensitivity of 0.214 V kPa^{-1}, a response time of 30 ms, a minimum resolution of 1.415 kPa, and the durability test over 30,000 cycles, MA-TENG exhibits excellent sensing capability over a range of 0 to 200 kPa. The DCNN tree as a decision model was built with the assistance of machine learning methods, and the severity indices (0 to 5) of head impact were assessed with an accuracy of 98% by algorithm optimization. An HIRS system was created to provide prediagnostic references in practical applications, for example, coaches and medical staff can judge whether to terminate a competition by the conclusions displayed by the smartphone in case of an athlete's injury. In addition, breakthroughs in the development of fully 3D printed sensing technologies could benefit pressure sensing devices with a variety of structures and applications. Accordingly, the developed MA-TENG sensing array is expected to bring great opportunities in the field of smart sports and wearable medical electronics.

MATERIALS AND METHODS

Fabrication of 3D printed materials

The biggest obstacle to the development of 3D printed TENG is functional printed materials. The market's available 3D printing raw materials are difficult to meet the requirements of TENG in terms of mechanical, conductivity, and triboelectric properties. We chose multiwalled carbon nanotube (purity > 98 weight %, outside diameter = 20 to 30 nm, and length = 10 to 30 μm; TIME NANO) as a nanofiller for polyurethane elastomers (83A, Badische Anilin-und-Soda-Fabrik, Germany) instead of metal to avoid

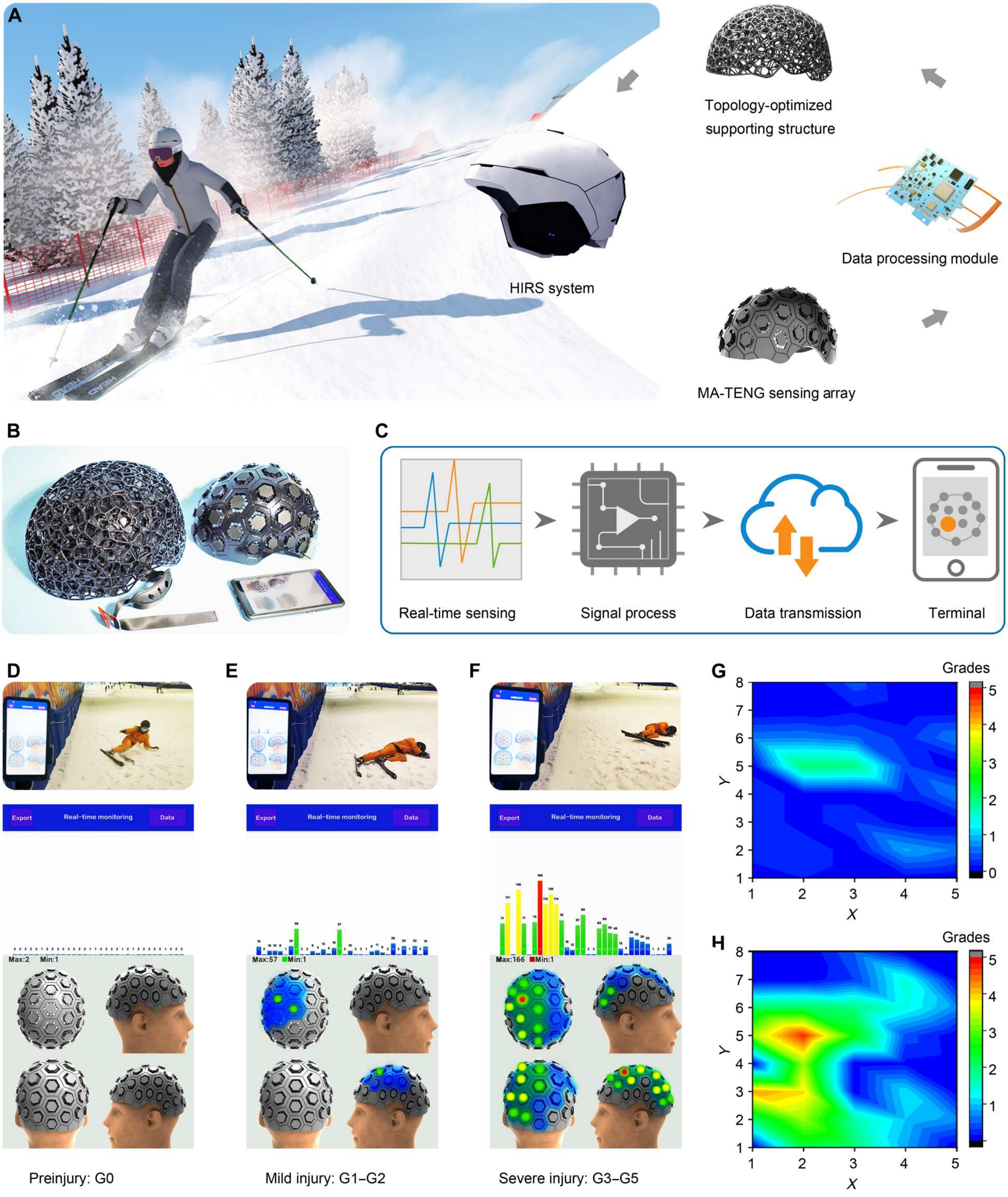

Fig. 5. Real-time monitoring of head impact by using the HIRS system. (**A**) Application scenario and components of the HIRS system. (**B**) Photograph of the HIRS system. (**C**) Operational scheme diagram of the HIRS system. (**D** to **F**) Photographs and visualized application screenshots of preinjury, mild injury, and severe injury when user falls down in a skiing accident. (**G**) 2D cloud map distribution at G1 and G2 of head impact. (**H**) 2D cloud map distribution at G3 to G5 of head impact.

interfacial cracks and difficult adhesion between metal and polymer. C-TPU was prepared by vacuum heating, mixing, and stirring, and mechanical extrusion (fig. S13). The temperature of each zone of the extruder is shown in table S4. C-TPU can reliably turn on the light-emitting diode light even when subjected to 148% tensile deformation (movie S4). The specific characterization of C-TPU samples is shown in figs. S14 to S16. Next, we introduced poly(vinylidene fluoride-*co*-hexafluoropropylene) (PVDF-HFP) to the TPU surface. This fluorinated resin is easier to gain electrons during contact separation and has high adhesion, thermal stability, and chemical stability. It will not peel, deform, and break after long-term mechanical work. Then, we compared the electrical output of various dielectric layers (fig. S17) and handled the elastic hemispheres. When compared to previous treatment, the T-TPU displayed 3-fold increase in voltage signal, a 5-fold increase in current signal, and a 10-fold increase in charge transfer (fig. S18).

Design of the data processing module

The module was designed by Altium Designer 20. Data transfer, data capture, and signal amplification are all accomplished by the module. The amplifier chip (TI, TLV2404) has a bandwidth of 5.5 kHz and a response speed of 1.8 ms. The amplifier receives pressure-modulated current signal inputs, and the amplified voltage outputs are subsequently sent to the main chip for sampling. The microprocessor (MSP430FR58671) has a sampling accuracy of 0.02 mV. The repeat-sequence-of-channels sampling conversion mode was used, and the sampling time was 8 μs. Then, using serial connection with a baud rate of 115,200, the data were sent to the Bluetooth chip. The Bluetooth chip (TI, CC2640) has low power consumption and a standby current of 1.1 μA. Cell phone refreshes data every 100 ms via Bluetooth. The received data can be forwarded to a computer or server for another procedure or temporarily retained in memory. The information is saved in ".txt" format to conserve memory. The cell phone terminal operating environment is based on Android.

Manufacturing of flex-PCB

The MA-TENGs and the data processing module are connected by the flex-PCB. The following are the specific fabrication specifications: Polyimide, the flex-PCB substrate, has a thickness of 0.13 mm and a 0.50-ounce copper plating. A sensitive dry layer is placed over the copper after the 32-channel pattern has been applied to the substrate. Next, the sensitive layer is subjected to ultraviolet light, and the unexposed portions can be erased using an etching procedure. The sensor is attached to the exposed copper end of the electrode windowed electrode, and the gold finger receptacle at the other end is connected to the data processing module.

Characterization and measurements

A step motor (E1100, LinMot) was used to simulate the impact forces from compression, shearing, and rotation (movie S5). The output performance of MA-TENG was measured by an electrometer (6517, KEITHLEY). The SEM images were taken by Hitachi field-emission SEM (SU 8020). The strain-stress tests were conducted by universal materials tester (YL-S71). Standardized tests of the MA-TENG sensing array are acquired by a multichannel measurement system (National Instruments). Work with data and data graphs with Origin 2021. Conductivity was measured by a Lenz Capacitor Resistance meter (4263B, Agilent). The head point cloud was collected by a 3D scanner (460+, BILIN). Machine learning algorithm programs including model training and prediction run on JMP and MATLAB 2018a.

Human individual statement

Individuals were all from the authors of this paper and gave informed consent to the publication of any form of personal data.

Supplementary Materials

This PDF file includes:

Supplementary Text 1 and 2
Figs. S1 to S18
Tables S1 to S4
Equation 1
Legends for movies S1 to S5

Other Supplementary Material for this manuscript includes the following:

Movies S1 to S5

REFERENCES AND NOTES

1. R. C. Gardner, K. Yaffe, Epidemiology of mild traumatic brain injury and neurodegenerative disease. *Mol. Cell. Neurosci.* **66**, 75–80 (2015).
2. D. H. Daneshvar, C. J. Nowinski, A. C. McKee, R. C. Cantu, The epidemiology of sport-related concussion. *Clin. Sports Med.* **30**, 1–17 (2011).
3. S. J. Preiss-Farzanegan, B. Chapman, T. M. Wong, J. Wu, J. J. Bazarian, The relationship between gender and postconcussion symptoms after sport-related mild traumatic brain injury. *PM R.* **1**, 245–253 (2009).
4. S. Stuart, A. Hickey, R. Morris, K. O'Donovan, A. Godfrey, Concussion in contact sport: A challenging area to tackle. *J. Sport Health Sci.* **6**, 299–301 (2017).
5. A. I. R. Maas, D. K. Menon, P. D. Adelson, N. Andelic, M. J. Bell, A. Belli, P. Bragge, A. Brazinova, A. Büki, R. M. Chesnut, G. Citerio, M. Coburn, D. J. Cooper, A. T. Crowder, E. Czeiter, M. Czosnyka, R. Diaz-Arrastia, J. P. Dreier, A.-C. Duhaime, A. Ercole, T. A. van Essen, V. L. Feigin, G. Gao, J. Giacino, L. E. Gonzalez-Lara, R. L. Gruen, D. Gupta, J. A. Hartings, S. Hill, J. Y. Jiang, N. Ketharanathan, E. J. O. Kompanje, L. Lanyon, S. Laureys, F. Lecky, H. Levin, H. F. Lingsma, M. Maegele, M. Majdan, G. Manley, J. Marsteller, L. Mascia, C. McFadyen, S. Mondello, V. Newcombe, A. Palotie, P. M. Parizel, W. Peul, J. Piercy, S. Polinder, L. Puybasset, T. E. Rasmussen, R. Rossaint, P. Smielewski, J. Söderberg, S. J. Stanworth, M. B. Stein, N. von Steinbüchel, W. Stewart, E. W. Steyerberg, N. Stocchetti, A. Synnot, B. Te Ao, O. Tenovuo, A. Theadom, D. Tibboel, W. Videtta, K. K. W. Wang, W. H. Williams, L. Wilson, K. Yaffe; InTBIR Participants and Investigators, Traumatic brain injury: Integrated approaches to improve prevention, clinical care, and research. *Lancet Neurol.* **16**, 987–1048 (2017).
6. J. Ko, M. A. Hemphill, D. Gabrieli, L. Wu, V. Yelleswarapu, G. Lawrence, W. Pennycooke, A. Singh, D. F. Meaney, D. Issadore, Smartphone-enabled optofluidic exosome diagnostic for concussion recovery. *Sci. Rep.* **6**, 31215 (2016).
7. K. Dong, Z. Wu, J. Deng, A. C. Wang, H. Zou, C. Chen, D. Hu, B. Gu, B. Sun, Z. L. Wang, A stretchable yarn embedded triboelectric nanogenerator as electronic skin for biomechanical energy harvesting and multifunctional pressure sensing. *Adv. Mater.* **30**, e1804944 (2018).
8. F. Yang, J. Li, Y. Long, Z. Zhang, L. Wang, J. Sui, Y. Dong, Y. Wang, R. Taylor, D. Ni, W. Cai, P. Wang, T. Hacker, X. Wang, Wafer-scale heterostructured piezoelectric bio-organic thin films. *Science* **373**, 337–342 (2021).
9. Z. Wang, J. An, J. Nie, J. Luo, J. Shao, T. Jiang, B. Chen, W. Tang, Z. L. Wang, A self-powered angle sensor at nanoradian-resolution for robotic arms and personalized medicare. *Adv. Mater.* **32**, e2001466 (2020).
10. A. Liu, Y. Long, J. Li, L. Gu, A. Karim, X. Wang, A. L. F. Gibson, Accelerated complete human skin architecture restoration after wounding by nanogenerator-driven electrostimulation. *J. Nanobiotechnol.* **19**, 280 (2021).
11. J. Luo, Z. Wang, L. Xu, A. C. Wang, K. Han, T. Jiang, Q. Lai, Y. Bai, W. Tang, F. R. Fan, Z. L. Wang, Flexible and durable wood-based triboelectric nanogenerators for self-powered sensing in athletic big data analytics. *Nat. Commun.* **10**, 5147 (2019).
12. J. Zhu, S. Ji, J. Yu, H. Shao, H. Wen, H. Zhang, Z. Xia, Z. Zhang, C. Lee, Machine learning-augmented wearable triboelectric human-machine interface in motion identification and virtual reality. *Nano Energy* **103**, 107766 (2022).

13. Y. Liu, W. Liu, Z. Wang, W. He, Q. Tang, Y. Xi, X. Wang, H. Guo, C. Hu, Quantifying contact status and the air-breakdown model of charge-excitation triboelectric nanogenerators to maximize charge density. *Nat. Commun.* **11**, 1599 (2020).
14. M. Zhu, Q. Shi, T. He, Z. Yi, Y. Ma, B. Yang, T. Chen, C. Lee, Self-powered and self-functional cotton sock using piezoelectric and triboelectric hybrid mechanism for healthcare and sports monitoring. *ACS Nano* **13**, 1940–1952 (2019).
15. H. Lee, H. E. Lee, H. S. Wang, S.-M. Kang, D. Lee, Y. H. Kim, J. H. Shin, Y.-W. Lim, K. J. Lee, B.-S. Bae, Hierarchically surface-textured ultrastable hybrid film for large-scale triboelectric nanogenerators. *Adv. Funct. Mater.* **30**, 2005610 (2020).
16. D. Liu, D. Zhang, Z. Sun, S. Zhou, W. Li, C. Li, W. Li, W. Tang, Z. L. Wang, Active-matrix sensing array assisted with machine-learning approach for lumbar degenerative disease diagnosis and postoperative assessment. *Adv. Funct. Mater.* **32**, 2113008 (2022).
17. J. An, P. Chen, Z. Wang, A. Berbille, H. Pang, Y. Jiang, T. Jiang, Z. L. Wang, Biomimetic hairy whiskers for robotic skin tactility. *Adv. Mater.* **33**, 2101891 (2021).
18. X. Pu, H. Guo, J. Chen, X. Wang, Y. Xi, C. Hu, Z. L. Wang, Eye motion triggered self-powered mechnosensational communication system using triboelectric nanogenerator. *Sci. Adv.* **3**, e1700694 (2017).
19. H. S. Wang, T. H. Im, Y. B. Kim, S. H. Sung, S. Min, S. H. Park, H. E. Lee, C. K. Jeong, J. H. Park, K. J. Lee, Flash-welded ultraflat silver nanowire network for flexible organic light-emitting diode and triboelectric tactile sensor. *APL Mater.* **9**, 061112 (2021).
20. S.-Z. Guo, K. Qiu, F. Meng, S. H. Park, M. C. McAlpine, 3D printed stretchable tactile sensors. *Adv. Mater.* **29**, 1701218 (2017).
21. S. H. Park, R. Su, J. Jeong, S.-Z. Guo, K. Qiu, D. Joung, F. Meng, M. C. McAlpine, 3D printed polymer photodetectors. *Adv. Mater.* **30**, 1803980 (2018).
22. H. Cui, D. Yao, R. Hensleigh, H. Lu, A. Calderon, Z. Xu, S. Davaria, Z. Wang, P. Mercier, P. Tarazaga, X. R. Zheng, Design and printing of proprioceptive three-dimensional architected robotic metamaterials. *Science* **376**, 1287–1293 (2022).
23. D. Joung, V. Truong, C. C. Neitzke, S.-Z. Guo, P. J. Walsh, J. R. Monat, F. Meng, S. H. Park, J. R. Dutton, A. M. Parr, M. C. McAlpine, 3D printed stem-cell derived neural progenitors generate spinal cord scaffolds. *Adv. Funct. Mater.* **28**, 1801850 (2018).
24. B. Chen, W. Tang, T. Jiang, L. Zhu, X. Chen, C. He, L. Xu, H. Guo, P. Lin, D. Li, J. Shao, Z. L. Wang, Three-dimensional ultraflexible triboelectric nanogenerator made by 3D printing. *Nano Energy* **45**, 380–389 (2018).
25. G. Liu, Y. Gao, S. Xu, T. Bu, Y. Xie, C. Xu, H. Zhou, Y. Qi, C. Zhang, One-stop fabrication of triboelectric nanogenerator based on 3D printing. *EcoMat.* **3**, e12130 (2021).
26. M. Peng, Z. Wen, L. Xie, J. Cheng, Z. Jia, D. Shi, H. Zeng, B. Zhao, Z. Liang, T. Li, L. Jiang, 3D printing of ultralight biomimetic hierarchical graphene materials with exceptional stiffness and resilience. *Adv. Mater.* **31**, 1902930 (2019).
27. H. Ouyang, Z. Liu, N. Li, B. Shi, Y. Zou, F. Xie, Y. Ma, Z. Li, H. Li, Q. Zheng, X. Qu, Y. Fan, Z. L. Wang, H. Zhang, Z. Li, Symbiotic cardiac pacemaker. *Nat. Commun.* **10**, 1821 (2019).
28. C. Li, D. Liu, C. Xu, Z. Wang, S. Shu, Z. Sun, W. Tang, Z. L. Wang, Sensing of joint and spinal bending or stretching via a retractable and wearable badge reel. *Nat. Commun.* **12**, 2950 (2021).
29. Y. Zou, P. Tan, B. Shi, H. Ouyang, D. Jiang, Z. Liu, H. Li, M. Yu, C. Wang, X. Qu, L. Zhao, Y. Fan, Z. L. Wang, Z. Li, A bionic stretchable nanogenerator for underwater sensing and energy harvesting. *Nat. Commun.* **10**, 2695 (2019).
30. J. Shao, M. Willatzen, Y. Shi, Z. L. Wang, 3D mathematical model of contact-separation and single-electrode mode triboelectric nanogenerators. *Nano Energy* **60**, 630–640 (2019).
31. D. Y. Park, D. J. Joe, D. H. Kim, H. Park, J. H. Han, C. K. Jeong, H. Park, J. G. Park, B. Joung, K. J. Lee, Self-powered real-time arterial pulse monitoring using ultrathin epidermal piezoelectric sensors. *Adv. Mater.* **29**, 1702308 (2017).
32. W. Li, J. Duan, J. Zhong, N. Wu, S. Lin, Z. Xu, S. Chen, Y. Pan, L. Huang, B. Hu, J. Zhou, Flexible THV/COC piezoelectret nanogenerator for wide-range pressure sensing. *ACS Appl. Mater. Interfaces* **10**, 29675–29683 (2018).
33. K. Parida, V. Bhavanasi, V. Kumar, R. Bendi, P. S. Lee, Self-powered pressure sensor for ultra-wide range pressure detection. *Nano Res.* **10**, 3557–3570 (2017).
34. C. Chen, Z. Wen, J. Shi, X. Jian, P. Li, J. T. W. Yeow, X. Sun, Micro triboelectric ultrasonic device for acoustic energy transfer and signal communication. *Nat. Commun.* **11**, 4143 (2020).
35. M. Ha, S. Lim, S. Cho, Y. Lee, S. Na, C. Baig, H. Ko, Skin-inspired hierarchical polymer architectures with gradient stiffness for spacer-free, ultrathin, and highly sensitive triboelectric sensors. *ACS Nano* **12**, 3964–3974 (2018).
36. G. Yao, L. Xu, X. Cheng, Y. Li, X. Huang, W. Guo, S. Liu, Z. L. Wang, H. Wu, Bioinspired triboelectric nanogenerators as self-powered electronic skin for robotic tactile sensing. *Adv. Funct. Mater.* **30**, 1907312 (2020).
37. Z. Zhao, Q. Huang, C. Yan, Y. Liu, X. Zeng, X. Wei, Y. Hu, Z. Zheng, Machine-washable and breathable pressure sensors based on triboelectric nanogenerators enabled by textile technologies. *Nano Energy* **70**, 104528 (2020).
38. K. M. Guskiewicz, J. P. Mihalik, V. Shankar, S. W. Marshall, D. H. Crowell, S. M. Oliaro, M. F. Ciocca, D. N. Hooker, Measurement of head impacts in collegiate football players: Relationship between head impact biomechanics and acute clinical outcome after concussion. *Neurosurgery* **61**, 1244–1252 (2007).

Acknowledgments

Funding: We acknowledge the support from National Natural Science Foundation of China (grant no. 52192610) and National Key R & D Project from Minister of Science and Technology (2021YFA1201601). **Author contributions:** Conceptualization: L.Z. and B.C. Methodology: L.Z. Investigation: L.Z., J.W., S.W., M.Z., and W.S. Visualization: L.Z. and J.W. Supervision: B.C. and Z.L.W. Writing—original draft: L.Z. and B.C. Writing—review and editing: L.Z., B.C., and Z.L.W. **Competing interests:** The authors declare that they have no competing interests. **Data and materials availability:** All data needed to evaluate the conclusions in the paper are present in the paper and/or the Supplementary Materials.

Submitted 3 January 2023
Accepted 14 April 2023
Published 17 May 2023
10.1126/sciadv.adg5152

Science Advances

Multiangle, self-powered sensor array for monitoring head impacts

Lulu Zu, Jing Wen, Shengbo Wang, Ming Zhang, Wuliang Sun, Baodong Chen, and Zhong Lin Wang

Sci. Adv., **9** (20), eadg5152.
DOI: 10.1126/sciadv.adg5152